analytical chemistry

pubs.acs.org/ac Article

Photocurrent Polarity Reversal Induced by Electron-Donor Release for the Highly Sensitive Photoelectrochemical Detection of Vascular Endothelial Growth Factor 165

Weisu Kong, Zhiyuan Xu, Tianrui Liu, Jianping Lei, and Huangxian Ju*

Cite This: *Anal. Chem.* 2023, 95, 16392−16397 Read Online

ACCESS | Metrics & More | Article Recommendations | Supporting Information

ABSTRACT: Photocurrent polarity reversal is a switching process between the anodic and cathodic pathways and is critical for eliminating false positivity and improving detection sensitivity in photoelectrochemical (PEC) sensing. In this study, we construct a PEC sensor with excellent photocurrent polarity reversal induced by ascorbic acid (AA) as an electron donor with the energy level matching the photoactive material zirconium metal−organic framework (ZrMOF). The ZrMOF-modified electrode demonstrates cathodic photocurrent in the presence of O_2 as an electron acceptor, while the anodic photocurrent is generated in the presence of AA, achieving photocurrent polarity reversal. By the in situ release of AA from AA-encapsulated apoferritin modified with DNA 2 (AA@APO-S2) as a detection tag in the presence of trypsin after the recognition of hairpin DNA-modified indium tin oxide to the reaction product of aptamer/DNA 1 with the target protein and the following rolling cycle amplification for introducing the detection tag to the sensing interface, the reversed photocurrent shows an enhanced photocurrent response to the target protein, leading to a highly sensitive PEC sensing strategy. This strategy realizes the detection of vascular endothelial growth factor 165 with good specificity, a wide linear range, and a low detection limit down to 5.3 fM. The actual sample analysis offers the detection results of the proposed PEC sensor comparable to those of commercial enzyme-linked immunosorbent assay tests, indicating the promising application of the photocurrent polarity reversal-based PEC sensing strategy in biomolecule detection and clinical diagnosis.

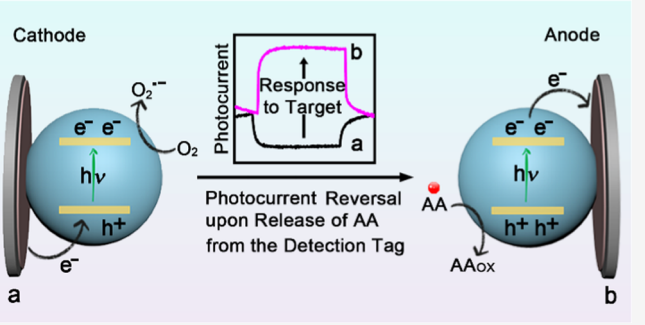

INTRODUCTION

Photoelectrochemical (PEC) detection is a highly sensitive and rapid analysis technique. It is generally achieved through photocurrent variation upon the recognition of a detection probe or a sensing interface to the target analyte.[1,2] However, the unsatisfactory sensitivity and anti-interference ability of "signal-off" or "signal-on" PEC detection systems limit their further applications. Hence, it is crucial to develop effective PEC sensing strategies with high sensitivity and detection accuracy.[3,4] In recent years, a sensing strategy of photocurrent polarity reversal has gained significant attention due to its ability to eliminate false-positive signals and its enhanced sensitivity.[5−9] Typically, Ren et al. employed small molecule-sensitized SnS_2 to obtain a photoanodic signal and avidin-functionalized $CuInS_2$ as a signal probe to realize signal reversal in the presence of cytokeratin 19 fragment 21−1.[8] Chen's group achieved photocurrent conversion by connecting the N-type semiconductor $AgInS_2$ with the P-type semiconductor CuO for a prostate-specific antigen assay.[9] Although breakthroughs have been made in the construction of the photocurrent polarity reversal strategy, the complex photoelectrode composition impedes efficient electron transfer and weakens the practicality of this strategy. The construction of a PEC sensing strategy with simple photoelectrode materials, highly efficient electron transfer, and stable photocurrent polarity reversal will be beneficial to the development of PEC sensing applications.

In the PEC process, the electron donor can consume photogenerated holes to prevent the recombination of electron−hole pairs and generate anodic photocurrent when the valence band (VB) position of the photoactive material is lower than the VB position of the electron donor.[10−13] In contrast, the conduction band (CB) position being higher than that of the electron acceptor can facilitate the reduction reaction to produce a cathodic photocurrent.[14−16] Overall, the generation of cathodic/anodic photocurrent requires a well-matched energy level between the photoelectrode material and the electron donor/acceptor.[17−20] Therefore, the addition of an electron donor/acceptor with a suitable energy band in the

Received: September 4, 2023
Revised: October 13, 2023
Accepted: October 18, 2023
Published: October 27, 2023

https://doi.org/10.1021/acs.analchem.3c03982
Anal. Chem. 2023, 95, 16392−16397

Scheme 1. Schematic Diagrams of (A) Release of S1 via the Recognition of Aptamer to $VEGF_{165}$ and (B) Preparation of AA-Encapsulated Apoferritin Modified with DNA 2 (AA@APO-S2). (C) Fabrication and Photocurrent Polarity Reversal Mechanism of the Proposed Photoelectrochemical Biosensor for $VEGF_{165}$

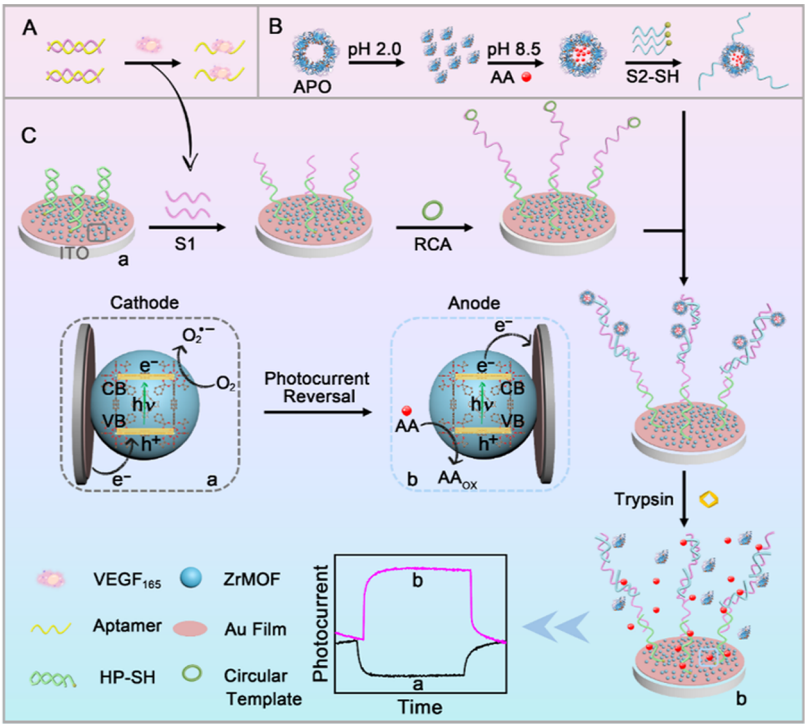

electrolyte can promote photocurrent enhancement. For example, Zhao et al. enhanced the anodic PEC performance of the MnO_2@Co_3O heterostructure by using ascorbic acid (AA) as an electron donor to consume the produced holes.[13] Zhang's team achieved cathodic photocurrent enhancement by using dissolved oxygen (O_2) as an electron acceptor.[14] Nevertheless, the formation of an insulating biomolecular layer on the PEC sensor inhibited electron transfer between the added electron sacrifice and the electrode surface.[21−23] To address this problem, this work designed an in situ release strategy of electron donor on the photoelectrode to realize photocurrent polarity reversal of metal−organic frameworks (MOFs), which is conducive to improving the precision and sensitivity of PEC detection.

MOF materials are a class of porous materials with a periodic structure and have attracted considerable attention due to their diverse structure and tunable band gap.[24−26] Their porous structure offers the possibility to facilitate the diffusion of electron donors and increase reaction sites for improving the electron transfer capability in PEC.[27−29] In this work, the photocurrent polarity reversal behavior of zirconium-based MOFs (ZrMOFs) was found in the presence of AA due to their matching band gaps. Through designing a PEC sensing interface with 40 nm $ZrMOF_{40}$ deposited with a gold film for the immobilization of hairpin DNA (Table S1) and a detection tag with AA-encapsulated apoferritin modified with DNA 2 (AA@APO-S2) for in situ AA release on the interface, a highly sensitive PEC sensing strategy was thus constructed. The in situ AA release was achieved in the presence of trypsin, which catalyzed the hydrolysis of apoferritin, after the recognition of hairpin DNA-modified indium tin oxide (ITO) to the reaction product S1 of aptamer/DNA 1 (Apt/S1) as a recognition probe with the target protein and the following rolling cycle amplification (RCA) for introducing the detection tag to the sensing interface (Scheme 1). Notably, the in situ release promoted the enrichment of AA in the pores of the framework material to shorten the electron transfer path and thus improved the PEC performance. Using vascular endothelial growth factor 165 ($VEGF_{165}$) as a target protein and its specific aptamer for the preparation of a recognition probe, the proposed PEC sensing method showed high detection sensitivity along with a wide concentration range and a low detection limit. The photocurrent polarity reversal provides a new diagram for accomplishing the highly sensitive detection of broad analytes.

EXPERIMENTAL SECTION

Preparation of ZrMOFs and AA@APO-S2. ZrMOFs with the space group *Pm*3*m* were synthesized by the solvothermal method.[30,31] The ZrMOF structure was similar to that in a previous report.[31] A mixture of zirconyl chloride octahydrate ($ZrOCl_2{\cdot}8H_2O$) (30 mg), tetrakis(4-carboxyphenyl)porphyrin (TCPP, 10 mg), and various quantities (360, 450, 630, and 750 mg) of benzoic acid (BA) was suspended in *N*,*N*-dimethylformamide (DMF, 10 mL) and heated in a round-bottomed flask at 90 °C for 5 h. The powders of $ZrMOF_{40}$, $ZrMOF_{100}$, $ZrMOF_{250}$, and $ZrMOF_{570}$ with sizes of about 40, 100, 250, and 570 nm, respectively, were obtained after washing with DMF several times, centrifuging, and subsequently drying under vacuum at 60 °C.

A 100 μL portion of apoferritin (APO, 25 mg mL^{-1}) was dispersed into 1.0 mL of PBS (0.01 M, pH 7.4), followed by the slow addition of 0.1 M HCl to adjust the pH to 2.0 and keep stirring for 20 min. Then, AA (100 μL, 0.5 M) was added dropwise and the pH was adjusted to 8.5 with 0.1 M NaOH.

https://doi.org/10.1021/acs.analchem.3c03982
Anal. Chem. 2023, 95, 16392−16397

The mixture was stirred for 2 h at room temperature to successfully encapsulate AA inside APO. Finally, excess AA was removed by dialysis three times in 0.01 M PBS (pH 7.4) for 24 h.[32] 200 μL of AA@APO was mixed with 60-fold moles of *m*-maleimidobenzoic acid *N*-hydroxy succinimide ester (MBS, 40 μL) and shaken for 2 h, and excess MBS was removed by ultrafiltration to obtain AA@APO-MBS. Meanwhile, 10 μM S2 (Table S1) was reduced with 200-fold moles of tris(2-carboxyethyl)phosphine (TCEP) in 0.01 M Tris-HCl (110 μL, pH 7.4) for 2 h. The reduced S2 was mixed with AA@APO-MBS and incubated for 2 h at room temperature to gain AA@APO-S2 and stored at 4 °C prior to use.[33]

Fabrication of the PEC Biosensor. The ITO glass substrate was washed ultrasonically in acetone, ethanol, and ultrapure water and dried at 50 °C for 3 h. 20 μL of a $ZrMOF_{40}$ dispersion (1.0 mg mL^{-1}) was then dropped on the ITO electrode with a geometric diameter of 0.5 cm ($ZrMOF_{40}$/ITO) to dry at 37 °C for 3 h. Afterward, the $ZrMOF_{40}$/ITO electrode was immersed in 1.0% $HAuCl_4$ solution for depositing the Au film on its surface at −0.2 V for 10 s. After hairpin DNA (HP) was treated with 0.01 M Tris-HCl (pH 7.4) containing 20 mM TCEP for 2 h to reduce the disulfide bond,[33] 10 μL of HP (2 μM) was dropped to the Au film-deposited $ZrMOF_{40}$/ITO electrode overnight at 4 °C, and then, 5 μL of 1-hexanethiol (0.1 mM) was dropped at room temperature for 40 min to block the nonspecific binding sites for obtaining the PEC sensing interface.

PEC Biosensing of $VEGF_{165}$. Apt/S1 was first prepared by incubating 100 μL of 2 μM aptamer and 100 μL of 2.2 μM S1 at 37 °C for 1 h, which was then mixed with 100 μL of $VEGF_{165}$ at 37 °C for 1 h. Afterward, 20 μL of the reaction product was dropped onto the PEC sensing interface and incubated for 1 h at 37 °C. The captured S1 was then used to perform the RCA by adding 10 μL of Padlock DNA (2 μM) on the electrode to anneal at 65 °C for 10 min and the mixture of T4 ligase (4 μL, 2 U $μL^{-1}$) and 10 × T4 buffer (6 μL) to incubate overnight at 16 °C. After inactivation of the T4 ligase at 65 °C for 10 min, the mixture of Phi29 polymerase (0.5 μL, 2 μM), 10 × Phi29 buffer (3.6 μL), and dNTPs (3 μL, 10 mM) was added on the electrode to incubate at 37 °C for 1 h. Finally, 10 μL of AA@APO-S2 solution was added onto the electrode to incubate at 37 °C for 1 h, which was immersed in 0.01 M PBS (pH 7.4) containing 5.0 μg mL^{-1} trypsin and 0.1 M NaCl to in situ release AA at AA@APO-S2/$ZrMOF_{40}$/ITO (Scheme 1), and the PEC measurements were performed at 0 V (vs Ag/AgCl) to avoid the effect of applied potential on polarity.

RESULTS AND DISCUSSION

Characterization of ZrMOFs. The transmission electron microscopic (TEM) images (Figures 1A and S1) and dynamic light scattering (DLS) measurements (Figures 1B and S2) of the synthesized ZrMOFs showed spherical structures and sizes of 40, 100, 250, and 570 nm, respectively (Table S2). The energy-dispersive spectroscopic (EDS) elemental mapping analysis confirmed the uniform distribution of C, N, and Zr elements in the frameworks (Figure S3). The successful preparation of ZrMOFs with different sizes was also verified by powder X-ray diffraction (PXRD) patterns (Figures 1C and S4), which showed the same crystallinity and corresponded well to the simulated peaks.[30] The microporous structure of $ZrMOF_{40}$ was verified by N_2 adsorption−desorption isotherms

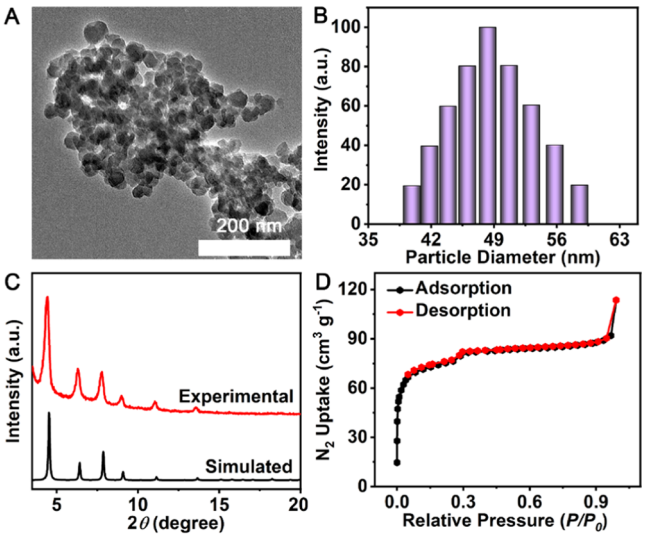

Figure 1. (A) TEM image, (B) DLS characterization, (C) PXRD pattern, and (D) N_2 adsorption−desorption isotherms of $ZrMOF_{40}$.

(Figure 1D), which revealed a typical type I isotherm with a Brunauer−Emmett−Teller (BET) surface area of 242 m^2 g^{-1}.

The X-ray photoelectron spectroscopic (XPS) survey spectrum of $ZrMOF_{40}$ further confirmed the presence of C, N, and Zr (Figure 2A). Moreover, two main peaks of the Zr 3d

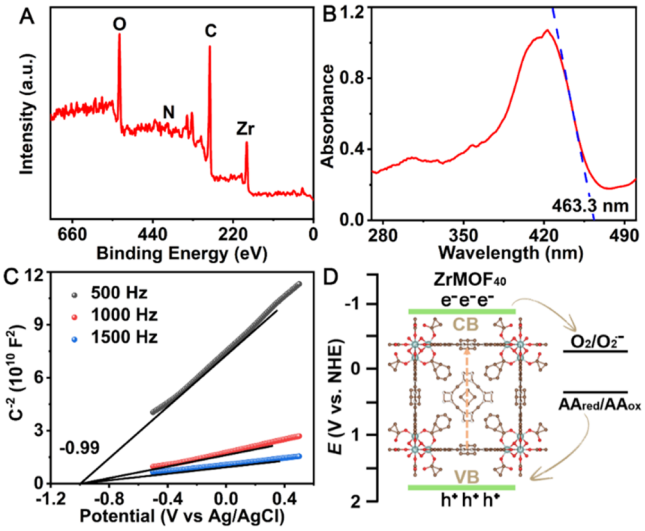

Figure 2. (A) XPS and (B) UV−vis DRS of $ZrMOF_{40}$. (C) Mott−Schottky plots of $ZrMOF_{40}$ in 0.2 M Na_2SO_4 solution (pH 7.0) at different frequencies. (D) Electron transfer process of the PEC biosensor.

spectrum at 182.0 and 184.4 eV (Figure S5), attributed to Zr $3d_{3/2}$ and Zr $3d_{5/2}$, respectively, confirmed the presence of Zr^{4+} ions.[34,35] In addition, the ultraviolet and visible (UV−vis) absorption spectrum displayed a broad absorption at 370−510 nm (Figure S6A), which corresponded to the unique electronic structure of the TCPP ligand.[36] The time-resolved photoluminescence spectrum of $ZrMOF_{40}$ at the excitation wavelength of 405 nm indicated a fluorescence lifetime of 2.1 ns (Figure S6B), verifying the ability of electron−hole pair separation.

Mechanism of Photocurrent Polarity Reversal. UV−vis diffuse reflectance spectrum (DRS) and the Mott−Schottky

https://doi.org/10.1021/acs.analchem.3c03982
Anal. Chem. 2023, 95, 16392−16397

plot were used to characterize the semiconductor properties of $ZrMOF_{40}$. The $ZrMOF_{40}$ showed an absorption edge (λ) of about 463.3 nm (Figure 2B), from which the band-gap width (E_g) of $ZrMOF_{40}$ was calculated to be 2.68 eV with the equation $E_g = 1240/\lambda$.[37] Furthermore, the flat band potential (E_{FB}) of $ZrMOF_{40}$ was evaluated using Mott−Schottky plots (Figure 2C) to be −0.99 V (vs Ag/AgCl). The positive slope indicated an N-type semiconductor, which had a CB potential (E_{CB}) of about 0.1 V more negative than the E_{FB}.[38] The E_{CB} value for $ZrMOF_{40}$ was roughly calculated to be −1.09 eV vs Ag/AgCl, that is, −0.89 eV vs the normal hydrogen electrode (NHE) ($E_{NHE} = E_{Ag/AgCl} + 0.197$). The VB value ($E_{VB}$) of $ZrMOF_{40}$ was calculated to be 1.79 eV by the equation $E_{VB} = E_{CB} + E_g$.[38] Thus, the electron transfer mechanism of the PEC process of $ZrMOF_{40}$ could be described in Figure 2D.

$ZrMOF_{40}$ first produced electron−hole pairs under light irradiation, and dissolved O_2 acted as an electron acceptor to be reduced to the superoxide radical ($O_2^{\bullet-}$) by the electrons at the CB energy level, which hindered the recombination of electrons and holes and generated cathodic photocurrent. In the presence of AA as an electron acceptor, the photogenerated holes could be depleted to produce the anodic photocurrent due to the fact that the oxidation potential (0.31 V) of AA was located between the band gaps of MOF,[39] leading to photocurrent polarity reversal. Moreover, the polarity reversed photocurrent showed the size dependence of ZrMOFs. $ZrMOF_{40}$-modified ITO showed a greater photoanodic response than ITOs modified by $ZrMOF_{100}$, $ZrMOF_{250}$, and $ZrMOF_{570}$ in 0.01 M PBS containing 0.1 M NaCl and 5.0 mM AA (Figure S7A) due to the shortened electron transfer distance. $ZrMOF_{40}$ was thus used for the construction of the following PEC biosensing strategy.

Feasibility of the PEC Biosensing Strategy. The target recognition of Apt/S1 was assessed by fluorescence measurements with the FAM labeled aptamer at the 3′ end and BHQ1 labeled S1 at the 5′ end. The fluorescence of FAM in the Apt/S1 complex was almost completely quenched by BHQ1 and could be restored after adding $VEGF_{165}$ in the solution (Figure 3A), demonstrating the specific recognition of the aptamer to $VEGF_{165}$ to release S1 from the complex.

The successful execution of S1 capture and RCA for introducing a detection tag was verified by polyacrylamide gel electrophoresis (PAGE) (Figure 3B). Lanes b, c, and d showed a single band of HP, S1, and aptamer, respectively, and the mixture of S1 and aptamer showed a weak band corresponding to S1 and a strong band at greater weight (lane e), indicating the presence of the Apt/S1 complex. Similarly, the mixture of S1 and hairpin DNA also showed a weak band corresponding to S1 and a strong band at greater weight (lane f), which was attributed to the hybridization of S1 with hairpin DNA, verifying the capture of S1 by the sensing interface. Compared to the above solutions, the RCA product showed a band with a significantly slower shift (lane g), indicating the formation of the RCA product with a high molecular weight.

Compared to bare ITO, $ZrMOF_{40}$/ITO exhibited a much greater cathodic photocurrent (Figure S7B and curve a in Figure 3C), which decreased gradually with the modification of HP, the capture of S1, and following RCA (Figure 3C, curves b and c) due to the inhibition of the formed insulating biomolecular layer to electron transfer. These results further demonstrated the successful execution of the S1 capture and RCA.

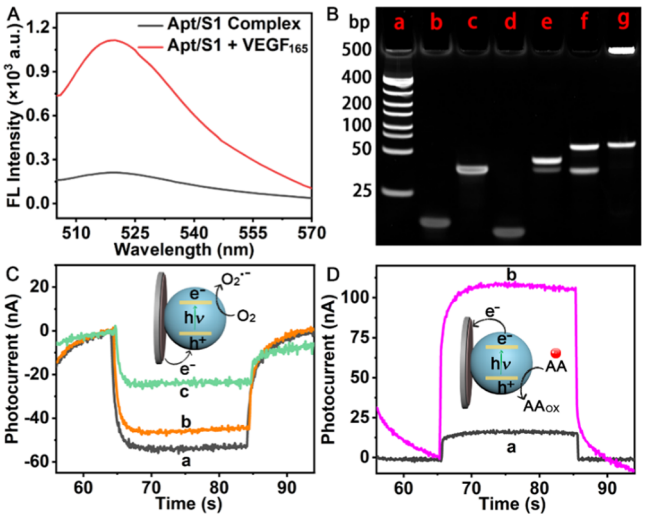

Figure 3. (A) Fluorescence spectra of Apt/S1 in the absence and presence of $VEGF_{165}$. Here, Apt is a 5′-FAM labeled aptamer, and S1 is 3′-BHQ1 labeled DNA 1. (B) PAGE analysis of DNA maker (a), HP (b), S1 (c), aptamer (d), S1 + Apt (e), S1 + HP (f), and RCA product (g). (C) Photocurrent responses of $ZrMOF_{40}$/ITO (a), HP/$ZrMOF_{40}$/ITO (b), and RCA product/$ZrMOF_{40}$/ITO (c) in 0.01 M pH 7.4 PBS containing 0.1 M NaCl. (D) Photocurrent responses of AA@APO-S2/$ZrMOF_{40}$/ITO at 0 V in 0.01 M pH 7.4 PBS containing 0.1 M NaCl (a) and with 5.0 μg mL^{-1} trypsin (b).

After introducing the detection tag to the RCA product to form AA@APO-S2/$ZrMOF_{40}$/ITO, significant photocurrent polarity reversal was observed (Figure 3D, curve a), which was attributed to the presence of a small number of AA on the tag surface. The polarity reversed photocurrent was greatly increased after the electrode was immersed in PBS containing trypsin (from 16.0 to 108.6 nA, Figure 3D, curve b), indicating the trypsin catalyzed hydrolysis of apoferritin to release more encapsulated AA.

The successive $ZrMOF_{40}$ coating, Au film deposition, hairpin DNA assembly, S1 capture, RCA, and introduction of the detection tag AA@APO-S2 were characterized by electrochemical impedance spectroscopy (EIS), which showed gradually decreasing electron transfer resistance (Figure S8), further confirming the fabrication and detection procedures of the PEC biosensor.

Optimization of Experimental Conditions. To acquire the best analytical performance, several important experimental factors, such as the wavelength for light irradiation, the MOF concentration for electrode preparation, the pH of the detection solution, the incubation time of Apt/S1 with $VEGF_{165}$, the concentration ratio of the aptamer to S1 for Apt/S1 preparation, and the trypsin concentration, were optimized. At a wavelength of 410 nm, $ZrMOF_{40}$ concentration of 1.0 mg mL^{-1} (20 μL), and pH 7.4, the $ZrMOF_{40}$/ITO showed the maximum photoanodic current in the presence of 5.0 mM AA (Figure S9). The incubation time of Apt/S1 with $VEGF_{165}$ and the concentration ratio of the aptamer to S1 were optimized with S1-BHQ1 with Apt-FAM, which gave the optimal values to be 1.0 h and 1.2, respectively (Figure S10). The maximum photoanodic current of AA@APO-S2/$ZrMOF_{40}$/ITO occurred at the trypsin concentration of 5.0 μg mL^{-1} (Figure S11). A higher trypsin concentration resulted in a very rapid degradation of the detection tag, which

https://doi.org/10.1021/acs.analchem.3c03982
Anal. Chem. 2023, 95, 16392−16397

was unfavorable to the response due to the removal of released AA from the electrode.

Analytical Performance for $VEGF_{165}$. Under optimal conditions, the photoanodic current increased with an increasing concentration of $VEGF_{165}$ (Figure S12) and treaded to the maximum value when the concentration was higher than 1000 pM (Figure 4A). The plot of photoanodic current vs the logarithm of $VEGF_{165}$ concentration displayed a linear relationship in the range of 0.01−500 pM with an equation of I = 62.10 + 12.79 lg $C_{VEGF165}$ (R^2 = 0.9940) (Figure 4B). The detection limit was calculated to be 5.3 fM and the S/N was 3, which was much lower than those using electrochemical and PEC methods (Table S3). Therefore, the PEC sensor based on the photocurrent polarity reversal of $ZrMOF_{40}$ proposed was a promising candidate for the detection of biomarkers.

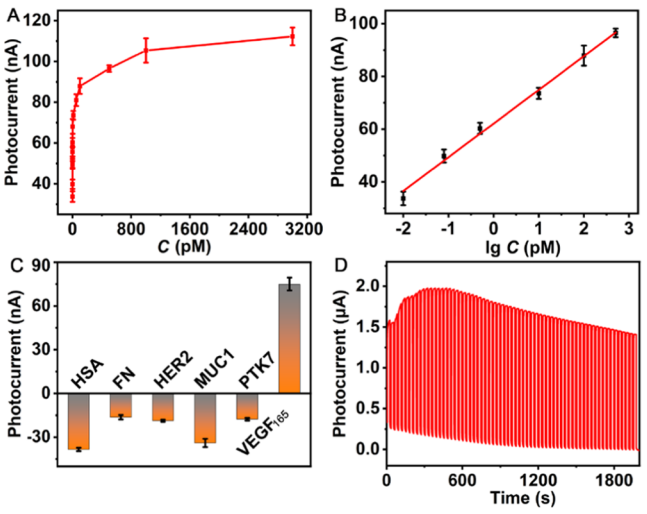

Figure 4. (A) Plot of photocurrent vs $VEGF_{165}$ concentration, and (B) the corresponding calibration curve for $VEGF_{165}$ determination in 0.01 M PBS (pH 7.4) containing 0.1 M NaCl. (C) Specificity of the proposed PEC sensing toward $VEGF_{165}$ at 10.0 pM and 1.0 nM interfering substances. The error bars are the standard deviation (SD) of three measurements. (D) Time-varying photocurrent response of the $ZrMOF_{40}$/ITO photoelectrode at 0 V in 0.01 M PBS containing 0.1 M NaCl and 5.0 mM AA.

The selectivity of the proposed $VEGF_{165}$ detection system was examined in the presence of possible interfering compounds such as human serum albumin (HAS), fibronectin (FN), human epidermal growth factor receptor 2 (HER2), mucin 1 (MUC1), and human protein tyrosine kinase-7 (PTK7). Only $VEGF_{165}$ showed polarity reversed photocurrent due to the specific recognition of the aptamer to the target (Figure 4C), indicating the excellent selectivity for $VEGF_{165}$ detection. Moreover, the photocurrent of $ZrMOF_{40}$/ITO remained stable during on−off cyclic light irradiation for 2000 s (Figure 4D), and the continuous illumination for 2 h did not obviously change the PXRD patterns of $ZrMOF_{40}$ (Figures 1C and S13A), indicating their excellent photostability. It also showed acceptable storage stability, and the photocurrent did not significantly change during a 10 day storage period (Figure S13B).

Serum Sample Detection. To investigate the potential applicability of the proposed PEC biosensing strategy in actual sample analysis, the amounts of $VEGF_{165}$ in the serum samples from different lung cancer patients were detected and compared to the results obtained from the commercial enzyme-linked immunosorbent assay (ELISA) method, which showed a linear equation of y = 0.2686 $C_{VEGF165}$ + 0.2359 (R^2 = 0.9930) (Figure 5A). Five serum samples from cancer patients were provided by the local hospital and diluted 100 times. Two methods gave the relative errors of −5.42−2.14% (Table S4). The detectability of the proposed method was satisfactorily comparable to that of commercially available ELISA kits (Figure 5B), suggesting its excellent reliability and precision for $VEGF_{165}$ detection.

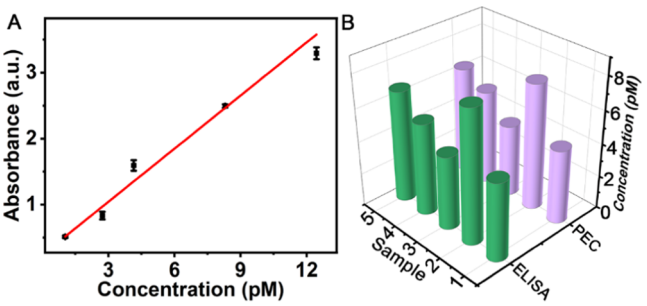

Figure 5. (A) ELISA calibration curve for the assessment of the $VEGF_{165}$ concentration. (B) Detection results with the PEC biosensor and ELISA methods.

CONCLUSIONS

An in situ release strategy of electron donors on a photoelectrode has been designed for realizing the photocurrent polarity reversal of MOFs and the highly sensitive PEC detection of biomolecules. The photocurrent polarity reversal behavior of ZrMOFs in the presence of AA, and its PEC mechanism, has been well described. A PEC biosensing strategy has been proposed by using $VEGF_{165}$ as the model target, its aptamer to prepare the recognition probe, and AA-encapsulated apoferritin modified with DNA 2 as the detection tag. The introduction of a detection tag to the interface RCA product and the in situ release of AA can greatly enhance the photoanodic response, leading to the excellent performance of the proposed PEC biosensing strategy with a wide detectable concentration range, an fM-level detection limit, high selectivity, acceptable stability, good accuracy, and satisfactory applicability. The photocurrent polarity reversal strategy triggered by in situ released electron donors provides a convenient method for highly accurate and sensitive bioanalysis.

ASSOCIATED CONTENT

Supporting Information

The Supporting Information is available free of charge at https://pubs.acs.org/doi/10.1021/acs.analchem.3c03982.

Experimental section (materials and reagents, apparatus); supporting figures (Figures S1−S13); and supporting tables (Tables S1−S4) (PDF)

AUTHOR INFORMATION

Corresponding Author

Huangxian Ju − *State Key Laboratory of Analytical Chemistry for Life Science, School of Chemistry and Chemical Engineering, Nanjing University, Nanjing 210023, P. R.*

https://doi.org/10.1021/acs.analchem.3c03982
Anal. Chem. 2023, 95, 16392−16397

China; orcid.org/0000-0002-6741-5302; Phone: +86-25-89683593; Email: hxju@nju.edu.cn

Authors

Weisu Kong − *State Key Laboratory of Analytical Chemistry for Life Science, School of Chemistry and Chemical Engineering, Nanjing University, Nanjing 210023, P. R. China*

Zhiyuan Xu − *State Key Laboratory of Analytical Chemistry for Life Science, School of Chemistry and Chemical Engineering, Nanjing University, Nanjing 210023, P. R. China*

Tianrui Liu − *State Key Laboratory of Analytical Chemistry for Life Science, School of Chemistry and Chemical Engineering, Nanjing University, Nanjing 210023, P. R. China*

Jianping Lei − *State Key Laboratory of Analytical Chemistry for Life Science, School of Chemistry and Chemical Engineering, Nanjing University, Nanjing 210023, P. R. China*; orcid.org/0000-0002-3594-180X

Complete contact information is available at: https://pubs.acs.org/10.1021/acs.analchem.3c03982

Notes

The authors declare no competing financial interest.

■ ACKNOWLEDGMENTS

This work was financially supported by the National Natural Science Foundation of China (21827812 and 21890741) and the Science and Technology Project of Nanjing City (202110023).

■ REFERENCES

(1) Ma, W.; Ma, H.; Peng, Y. Y.; Tian, H.; Long, Y. T. *Nat. Protoc.* **2019**, *14*, 2672−2690.
(2) Ye, X.; Wang, X.; Kong, Y.; Dai, M.; Han, D.; Liu, Z. *Angew. Chem., Int. Ed.* **2021**, *60*, 11774−11778.
(3) Zhao, W. W.; Xu, J. J.; Chen, H. Y. *Chem. Soc. Rev.* **2015**, *44*, 729−741.
(4) Zhou, Y.; Yin, H.; Ai, S. *Coord. Chem. Rev.* **2021**, *447*, 214165.
(5) Fu, Y.; Xiao, K.; Zhang, Q.; Zhang, X.; Du, C.; Chen, J. *Anal. Chem.* **2022**, *94*, 1874−1881.
(6) Cai, Q.; Yin, T.; Ye, Y.; Jie, G.; Zhou, H. *Anal. Chem.* **2022**, *94*, 5814−5822.
(7) Chen, X.; Yin, M.; Ge, R.; Wei, J.; Jiao, T.; Chen, Q.; Oyama, M.; Chen, Q. *Anal. Chem.* **2023**, *95*, 2698−2705.
(8) Zhang, J. H.; Xue, X. D.; Du, Y. Z.; Zhao, J. X.; Ma, H. M.; Ren, X.; Wei, Q.; Ju, H. X. *Anal. Chem.* **2022**, *94*, 12368−12373.
(9) Fu, Y.; Xiao, K.; Zhang, X.; Du, C.; Chen, J. *Anal. Chem.* **2021**, *93*, 1076−1083.
(10) Jiang, L.; Du, J.; Xu, H.; Zhuo, X.; Ai, J.; Zeng, J.; Yang, R.; Xiong, E. *Anal. Chem.* **2023**, *95*, 1193−1200.
(11) Ma, X.; Kang, J.; Wu, Y.; Pang, C.; Li, S.; Li, J.; Xiong, Y.; Luo, J.; Wang, M.; Xu, Z. *Chem. Eng. J.* **2023**, *469*, 143888.
(12) Yu, W.; Mo, F.; Guo, J.; Yang, Y.; Jin, Y.; Fu, Y. *Anal. Chem.* **2023**, *95*, 12097−12103.
(13) Zhao, D.; Geng, C.; Liu, X.; Jin, X.; Zhao, Z.; Liu, Y.; Alwarappan, S. *Biosens. Bioelectron.* **2023**, *237*, 115368.
(14) Zhang, G. Y.; Y, H.; Shan, D.; Su, G. F.; Cosnier, S.; Zhang, X. J. *Anal. Chem.* **2016**, *88*, 11207−11212.
(15) Xu, Y. T.; Yu, S. Y.; Zhu, Y. C.; Fan, G. C.; Han, D. M.; Qu, P.; Zhao, W. W. *TrAC, Trends Anal. Chem.* **2019**, *114*, 81−88, DOI: 10.1016/j.trac.2019.03.002.
(16) Wang, H.; Zhang, B.; Zhao, F.; Zeng, B. *ACS Appl. Mater. Interfaces* **2018**, *10*, 35281−35288.
(17) Abdi, G.; Alluhaibi, L.; Kowalewska, E.; Mazur, T.; Mech, K.; Podborska, A.; Sławek, A.; Tanaka, H.; Szaciłowski, K. *Coord. Chem. Rev.* **2023**, *487*, 215155.
(18) Nam, D. H.; Ryu, G. M.; Kuk, S. K.; Son, E.; Park, C. *Appl. Catal. B* **2016**, *198*, 311−317, DOI: 10.1016/j.apcatb.2016.05.077.
(19) Deng, J.; Su, Y.; Liu, D.; Yang, P.; Liu, B.; Liu, C. *Chem. Rev.* **2019**, *119*, 9221−9259.
(20) Ruan, Y. F.; Chen, F. Z.; Xu, Y. T.; Zhang, T. Y.; Yu, S. Y.; Zhao, W. W.; Jiang, D.; Chen, H. Y.; Xu, J. J. *Angew. Chem.* **2021**, *133*, 1−5.
(21) Tan, Y.; Wang, Y.; Li, M.; Ye, X.; Wu, T.; Li, C. *Biosens. Bioelectron.* **2017**, *91*, 741−746.
(22) Liu, A.; Yin, K.; Mi, L.; Ma, M.; Liu, Y.; Li, Y.; Wei, W.; Zhang, Y.; Liu, S. *Anal. Chim. Acta* **2017**, *973*, 82−90.
(23) Qu, P.; Li, C. J.; Hu, J.; Gao, G.; Lin, P.; Zhao, W. W. *Anal. Chem.* **2023**, *95*, 9983−9989.
(24) Zang, Y.; Lei, J. P.; Ju, H. X. *Biosens. Bioelectron.* **2017**, *96*, 8−16.
(25) Zhang, D. S.; Gao, Q.; Chang, Z.; Liu, X. T.; Zhao, B.; Xuan, Z. H.; Hu, T. L.; Zhang, Y. H.; Zhu, J.; Bu, X. H. *Adv. Mater.* **2018**, *30*, 1804715.
(26) Huang, N. Y.; He, H.; Liu, S.; Zhu, H. L.; Li, Y. J.; Xu, J.; Huang, J. R.; Wang, X.; Liao, P. Q.; Chen, X. M. *J. Am. Chem. Soc.* **2021**, *143*, 17424−17430.
(27) Wang, Q.; Astruc, D. *Chem. Rev.* **2020**, *120*, 1438−1511.
(28) Jiang, H.; Alezi, D.; Eddaoudi, M. *Nat. Rev. Mater.* **2021**, *6*, 466−487.
(29) Jin, Z.; Zhu, X.; Wang, N.; Li, Y.; Ju, H. X.; Lei, J. P. *Angew. Chem., Int. Ed.* **2020**, *59*, 10446−10450.
(30) Park, J.; Jiang, Q.; Feng, D.; Mao, L.; Zhou, H. C. *J. Am. Chem. Soc.* **2016**, *138*, 3518−3525.
(31) Morris, W.; Volosskiy, B.; Demir, S.; Gándara, F.; McGrier, P. L.; Furukawa, H.; Cascio, D.; Stoddart, J. F.; Yaghi, O. M. *Inorg. Chem.* **2012**, *51*, 6443−6445.
(32) Yin, H.; Wang, M.; Zhou, Y.; Zhang, X.; Sun, B.; Wang, G.; Ai, S. *Biosens. Bioelectron.* **2014**, *53*, 175−181.
(33) Ao, H.; Chen, W.; Wu, J.; Xiao, W.; Ju, H. X. *Commun. Biol.* **2022**, *5*, 308 DOI: 10.1038/s42003-022-03283-2.
(34) Dong, W.; Li, Z.; Wen, W.; Liu, B.; Wen, G. *ACS Appl. Mater. Interfaces* **2021**, *13*, 57497−57504.
(35) Jin, P.; Wang, L.; Ma, X.; Lian, R.; Huang, J.; She, H.; Zhang, M.; Wang, Q. *Appl. Catal., B* **2021**, *284*, 119762.
(36) Jiang, Z. W.; Zou, Y. C.; Zhao, T. T.; Zhen, S. J.; Li, Y. F.; Huang, C. Z. *Angew. Chem., Int. Ed.* **2020**, *59*, 3300−3306.
(37) Zhang, N.; Ruan, Y. F.; Zhang, L. B.; Zhao, W. W.; Xu, J. J.; Chen, H. Y. *Anal. Chem.* **2018**, *90*, 2341−2347.
(38) Wang, S.; Chai, Y.; Yuan, R.; Liu, H. *Anal. Chem.* **2023**, *95*, 4896−4903.
(39) Ping, J.; Wu, J.; Wang, Y.; Ying, Y. *Biosens. Bioelectron.* **2012**, *34*, 70−76.